Noise-Aware Adaptation of Vision Language Models for Single-photon Image Understanding

Anonymous authors
Paper under double-blind review

Abstract

Single-photon LiDAR enables high-resolution depth imaging under extreme photon-limited conditions, making it attractive for low-light and long-range 3D perception. Beyond depth reconstruction, semantic understanding from single-photon images remains challenging due to limited data and sensitivity to noise-induced appearance variation. In this work, we present a noise-aware adaptation framework that transfers large-scale vision-language models, such as CLIP, from natural RGB images to the novel modality of single-photon depth images for few-shot classification. We introduce a lightweight Noise Adapter that modulates CLIP visual features using summary statistics derived from raw single-photon histograms. This design helps decouple imaging noise from semantics, enabling more robust prediction under varying noise levels. Furthermore, we leverage the learned modulation pattern to guide feature-level augmentation, simulating feature changes caused by noise and improving generalization in the low-data regime. To the best of our knowledge, this is the first work to explicitly integrate noise-awareness into pre-trained model adaptation for single-photon images. Experiments on both synthetic and real single-photon datasets show that our method improves accuracy over baselines, with an average improvement of 3% over the best baseline. These results highlight the importance of modeling physical noise in photon-limited imaging and demonstrate the potential of leveraging vision models pre-trained on conventional modalities to improve performance on single-photon depth data with limited supervision.

1 Introduction

Single-photon avalanche diode (SPAD) LiDAR systems have emerged as a powerful solution for depth imaging in photon-starved environments (Hadfield, 2009; Halimi et al., 2019; McCarthy et al., 2025; Chan et al., 2024). Their ability to detect individual photons with picosecond timing resolution enables high-precision 3D reconstruction under low-light (Yang et al., 2015) or long-range conditions (Li et al., 2021), making them particularly attractive for applications such as autonomous navigation, robotics, and environmental sensing (Degnan, 2016; Rapp et al., 2020; Shangguan et al., 2023). While existing research focuses on improving depth reconstruction (Tachella et al., 2019; Malik et al., 2023), there is a growing interest in pushing SPAD imaging beyond geometry toward semantic understanding (Suonsivu et al., 2025; Axelsson, 2024; Zhang et al., 2025). Extending SPAD depth imaging beyond geometric reconstruction to semantic classification could significantly enhance the applicability of SPAD-based perception systems.

However, achieving reliable semantic understanding from SPAD images remains challenging, primarily due to limited data availability (Li et al., 2024; Hong et al., 2023). Unlike conventional RGB datasets, collecting and annotating SPAD data is significantly more costly, especially under diverse imaging conditions with varying photon counts and background illumination. Models trained on scarce labeled data often suffer from limited generalization capacity (Zhai et al., 2022). Moreover, SPAD images exhibit substantial appearance variations caused by photon-level noise, such as low photon counts and background contamination, as shown in Figure 1. Under these conditions, models struggle to disentangle noise-induced variations from true semantic differences, further degrading recognition performance (Suonsivu et al., 2025).

Large vision-language models (VLMs), such as CLIP, have recently shown strong generalization performance in low-data regimes by learning aligned image-text representations from massive RGB datasets (Radford et al., 2021; Li et al., 2023). These models enable accurate classification with only a few labeled examples by adapting lightweight modules while keeping the backbone frozen. This success in RGB image domains motivates us to explore whether similar adaptation strategies can be extended to SPAD-based semantic understanding. Although SPAD depth images differ significantly from RGB images, they often preserve coarse geometric patterns and depth structure that can support transferable visual representations (Auty & Mikolajczyk, 2023; Huang et al., 2023). Adapting VLMs to SPAD images could therefore offer a powerful and data-efficient solution for semantic interpretation in low-photon regimes.

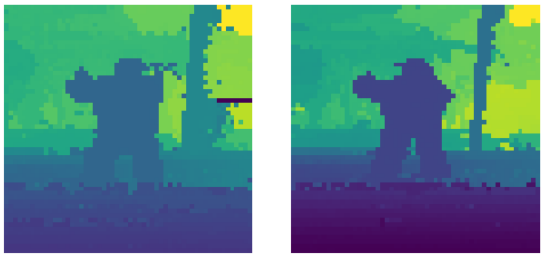

(a) Low photon count (b) High photon count

Figure 1: Examples of SPAD depth images under varying imaging conditions. Images are drawn from the SPAD real dataset (Zhang et al., 2025) and correspond to the same scene captured with different average photon counts per pixel.

Several recent adaptation methods have proposed lightweight mechanisms to adapt pre-trained VLM to downstream tasks (Zhou et al., 2022b; Gao et al., 2024; Zhang et al., 2022). However, they do not account for the unique characteristics of SPAD data, where imaging conditions, such as photon count and signal-background ratio, can strongly influence appearance. As a result, directly applying these methods to SPAD imagery may lead to degraded performance under noise variation. This motivates us to develop a noise-aware adaptation framework tailored to the characteristics of SPAD data.

We propose a noise-aware adaptation framework that integrates physically interpretable noise descriptors into the adaptation process. Specifically, we extract two summary statistics, the average detected photons per pixel and the estimated signal-to-background ratio (SBR), from the raw SPAD histograms. These descriptors are fed into a learnable gating module that modulates the frozen CLIP visual features, enabling the model to suppress noise-sensitive feature dimensions and emphasize robust ones. Building upon this mechanism, we further introduce a feature-level augmentation strategy, Gate-Guided Feature Augmentation (GGFA). This approach perturbs the input features along dimensions identified as noise-sensitive by the learned gating pattern, thereby simulating realistic appearance shifts caused by changes in imaging conditions. By injecting such variations during training, our framework enhances generalization to unseen noise patterns.

To the best of our knowledge, this is the first work to explicitly incorporate physical noise modeling into vision-language model adaptation for SPAD images. Beyond the specific SPAD context, our approach offers a practical direction for extending large-scale pre-trained models to novel sensing modalities in a label-efficient manner, highlighting the broader value of conditioning adaptation modules on physical acquisition conditions. Our contributions are three-fold: (1) We propose a Noise Adapter that feeds physical noise descriptors into a gating module to selectively modulate CLIP features, enabling adaptation that is informed by imaging conditions. (2) We observe that the learned gating vector captures per-dimension noise sensitivity and leverage this insight to design the GGFA strategy, which improves generalization by simulating noise-induced feature shifts. (3) We validate our approach on both synthetic and real SPAD datasets, where it consistently outperforms existing adapter tuning methods.

2 Related Works

2.1 Semantic Understanding of Single-photon Lidar Data

Single-photon LiDAR systems have primarily been studied for depth estimation and 3D reconstruction under extreme conditions (Legros et al., 2020; Malik et al., 2023; Luo et al., 2025). However, the semantic understanding of SPAD data remains largely unexplored. To promote research in this area, the Time-Resolved MNIST dataset was introduced as a simulated SPAD dataset for single-photon recognition, demonstrating how varying photon flux levels impact CNN recognition accuracy (Suonsivu et al., 2025).

Many existing methods adapt architectures originally developed for RGB images to noisy, low-resolution SPAD data, addressing tasks like object detection and human activity recognition under photon-starved conditions (MoraMartin et al., 2024; Li et al., 2024). A recent study further integrates active learning to enhance model performance using fewer labeled examples (Zhang et al., 2025). However, these approaches rely on reconstructed depth images, neglecting richer noise information in raw SPAD histograms. Some recent works directly utilize raw SPAD data for classification and detection without intermediate depth reconstruction (Hong et al., 2023; Zhu et al., 2020). Yet data structures of raw SPAD data significantly differ from RGB images, making it difficult to leverage models pre-trained on RGB images.

To bridge this gap, we propose a lightweight noise adapter that incorporates physically interpretable noise descriptors to capture rich information from raw SPAD histograms, while enabling effective adaptation of powerful vision-language models pre-trained on large-scale RGB datasets.

2.2 Lightweight Adaptation of Vision-Language Models

Recent large-scale vision-language models (VLMs) have demonstrated impressive zero-shot and few-shot generalization capabilities by learning robust image-text alignment from massive datasets (Radford et al., 2021; Li et al., 2023). Existing lightweight adaptation approaches typically fall into two main categories: prompt-tuning methods and adapter tuning.

Prompt tuning methods optimize a small set of learnable parameters to adapt the input of a frozen backbone, either through learnable textual prompts (Zhou et al., 2022b;a) or through visual prompts (Jia et al., 2022; Zeng et al., 2024; Han et al., 2023). Adapter tuning, in contrast, modifies the representations produced by the pre-trained encoder. Some approaches train lightweight modules on top of the frozen backbone (Gao et al., 2024; Huang et al., 2024). Other methods adopt cache-based models that store key-value representations derived from the few-shot training set. These caches can be used either as fixed non-parametric memories or further optimized as learnable components to enhance matching performance at test time (Zhang et al., 2022; Song et al., 2023; Zhu et al., 2023; Udandarao et al., 2023).

Despite these advances, current adaptation methods are predominantly tailored toward RGB imagery. Extending these adaptation frameworks to novel sensor modalities, such as SPAD depth images, poses unique challenges due to the distinct physical noise characteristics. Addressing these challenges requires methods capable of explicitly modeling sensor-specific variability alongside semantic content.

3 Preliminary: Physical Modeling of Single-Photon Noises

3.1 The Physics of Single-photon Imaging

Single-photon LiDAR operates by emitting pulsed laser signals, employs a single-photon avalanche diode (SPAD) to capture echo signals, combines with time-correlated single-photon counting to record temporal information of reflected photons, and derives target depth and reflectivity through analyzing photon statistical characteristics (Hadfield, 2009; McCarthy et al., 2025).

Specifically, for each pixel (i, j) of the target scene, we emit a pulsed laser beam with temporal waveform $s(t)$. The transient photon flux $\Phi_{i,j}(t)$ at the corresponding coordinate can be detected by SPAD arrays, given by Eq. 1:

$$\Phi_{i,j}(t) = \eta\alpha_{i,j}[s(t - \frac{2z_{i,j}}{c}) + b] + d, \tag{1}$$

where η is the quantum efficiency of the single photon detector, $\alpha_{i,j}$ is the reflectivity of the target object, $z_{i,j}$ is the depth of the target object, c is the speed of light, b is the ambient light intensity, and d is the dark count of the detector.

When the light flux is very low, the response of the SPAD detector (photon count histogram) can be considered as a non-uniform Poisson process as Eq. 2:

$$H_{i,j}(k) \sim \mathcal{P}\left(N\Phi_{i,j}(t)\right), \tag{2}$$

where $k = 1, \ldots, K$ represents the time-bins, N is the pulse repetition period (Rapp & Goyal, 2017). Each time bin corresponds to a fixed photon arrival interval determined by the system's bin duration Δt. Upon completing the full scan of the target scene, the histogram data from all pixel positions collectively form a matrix H. Then, single-photon imaging algorithms are used to recover the target's depth and reflectivity from the H (Tachella et al., 2019; Yao et al., 2022).

3.2 Exploiting Physical Noise for Image Understanding

Single-photon LiDAR captures depth information by recording the arrival times of photons at each pixel location as a histogram H. The observed photon counts are influenced by multiple imaging factors, including signal strength, background illumination, and total exposure. These factors vary across conditions and scenes, leading to significant visual changes in the reconstructed depth images. While conventional imaging algorithms (Tachella et al., 2019; Yao et al., 2022) recover depth estimates from H, downstream recognition models that operate solely on these depth maps typically overlook the detailed noise statistics inherent in the raw photon histograms. This limits their ability to distinguish between semantic variations and appearance shifts induced by different noise conditions.

To address this issue, we extract a compact noise embedding from H, capturing two physically interpretable descriptors: the average detected photon count and the estimated signal-to-background ratio (SBR). These descriptors reflect meaningful properties of the imaging process: photon count relates to signal sparsity, while SBR quantifies the proportion of useful signal relative to ambient noise. Crucially, both can be derived from the raw histogram data without requiring additional supervision or calibration. By integrating these descriptors into the downstream adaptation process, we enable the model to condition its predictions on imaging context—helping it decouple semantic information from noise-induced variations. This forms the basis of our noise-aware adaptation framework, detailed in the following sections.

4 Method

In this section, we formalize a framework for adapting a pre-trained vision–language model (VLM) to the unseen SPAD-LiDAR depth image modality. Our goal is to transfer rich semantic knowledge from the pre-training domain (RGB images) to SPAD data, while explicitly accounting for the unique noise characteristics of SPAD imaging. We address two key challenges: (1) the substantial distribution shift between the pre-training domain (natural RGB images) and the target SPAD depth images, and (2) strong intra-class appearance variations in SPAD images caused by photon-level noise under varying imaging conditions.

To tackle these challenges, we propose a noise-aware adaptation framework consisting of three main components: (1) Noise-Embedding Extraction, (2) Noise Adapter, and (3) Gate-Guided Feature Augmentation (GGFA). In the following subsections, we first formalize the problem setup and present the overall framework, and then describe each component in detail.

4.1 Overall Framework

We denote the available SPAD dataset as $\mathcal{D} = (H^i, I^i, y^i)_{i=1}^N$, where $H^i \in \mathbb{R}^{M\times W\times B}$ is the raw SPAD histogram, $I^i \in \mathbb{R}^{M\times W}$ is the corresponding depth image reconstructed from H^i via a SPAD imaging algorithm (Yao et al., 2022), and y^i is the associated label. Each histogram records photon counts over B time bins at each of the $M \times W$ pixels. The reconstructed depth image I^i serves as the input to the visual encoder, while the raw histogram H^i is used to extract noise embeddings.

Our method leverages the strong semantic priors encoded in the frozen CLIP visual encoder $f_V(\cdot)$, while explicitly modeling the impact of noise. The overall framework is illustrated in Figure 2. For each SPAD image, we first extract a global noise embedding z from the raw histogram H^i, capturing key imaging

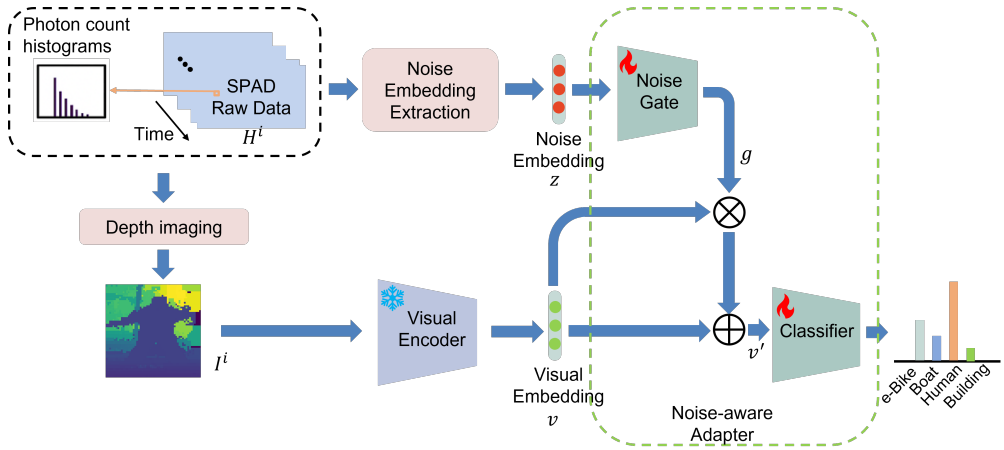

Figure 2: Overview of our noise-aware adaptation framework for SPAD depth images. A noise embedding extracted from the SPAD raw data modulates visual features obtained from the depth image via a noise-gated adapter. The modulated features are used for classification.

condition statistics. This noise embedding is then used to modulate the visual feature $v = f_V(I^i)$ through a learnable gating mechanism, producing a noise-aware feature representation. Additionally, we introduce a Gate-Guided Feature Augmentation (GGFA) strategy that generates realistic feature perturbations guided by the learned gating behavior, further improving model robustness to noise-induced variation. In the following sections, we describe each component of our method in detail.

4.2 Noise Embedding Extraction

We first describe how to extract a noise embedding from the raw SPAD histogram, summarizing each sample's imaging condition as input to the noise adapter. Given a SPAD histogram H^i, we compute a global noise embedding $z \in \mathbb{R}^2$ consisting of two scalar statistics: the average number of detected photons per pixel, and an estimated signal-to-background ratio (SBR). The average photon count per pixel, $\bar{c}_{\text{pix}}$, is computed as the total number of detected photons divided by the number of pixels ($M \times W$), providing a coarse measure of signal strength and imaging quality. Throughout this paper, we use the overline notation (e.g., $\bar{c}_{\text{pix}}$) to indicate spatial averaging across all pixels.

To estimate SBR, we leverage the depth image I^i reconstructed from H^i using a SPAD imaging algorithm (Yao et al., 2022). For each pixel (x, y), we first identify the expected signal arrival bin as $p(x, y) = \text{round}(2I^i(x, y)/(c\Delta t))$, where c denotes the speed of light and Δt is the bin duration. We then define a signal window of size w centered around $p(x, y)$ and compute the number of signal photons as Eq. 3:

$$c_{\text{sig}}(x, y) = \sum_{b=p(x,y)-w}^{p(x,y)+w} H^i(x, y, b). \tag{3}$$

The background photon count is computed by subtracting the estimated signal photons from the total count at each pixel, i.e., $c_{\text{bg}}(x, y) = \sum_{b=1}^{B} H^i(x, y, b) - c_{\text{sig}}(x, y)$. Then, the per-pixel SBR is computed as Eq. 4:

$$\text{SBR}(x, y) = \frac{c_{\text{sig}}(x, y)}{c_{\text{bg}}(x, y) + \epsilon}, \tag{4}$$

where ϵ is a small constant to prevent division by zero. The global SBR is obtained by averaging SBR(x,y) across all pixels, denoted as $\overline{\text{SBR}}$. Finally, the global noise embedding is defined as $z = [\bar{c}_{\text{pix}};\ \overline{\text{SBR}}]$. The resulting noise embedding z enables the noise adapter to modulate visual features according to the imaging conditions.

4.3 Noise Adapter

To address the impact of noise on SPAD image appearance, we introduce a Noise Adapter that explicitly leverages a noise embedding z to guide the modulation of CLIP visual features. As illustrated in Figure 2, this module comprises two components: a noise-conditioned gating network and a downstream classification head. Given a pre-trained visual feature $v \in \mathbb{R}^D$ and the noise embedding $z \in \mathbb{R}^2$, we first compute a per-dimension gating vector $g \in [0,1]^D$ via a multilayer perceptron (MLP): $g = \text{MLP}(z)$. The gating vector modulates the visual feature v through an element-wise operation with a residual connection, as shown in Eq. 5, where $\odot$ denotes element-wise multiplication.

$$v' = v \odot g + v. \tag{5}$$

This residual formulation preserves the structure of the pre-trained visual feature while enabling noise-aware modulation, which promotes stable training and mitigates degradation of semantic representations under varying noise conditions. The modulated feature v' is then passed through a classification head to produce semantic predictions.

By explicitly conditioning feature adaptation on noise descriptors, the proposed Noise Adapter enhances robustness to appearance variations caused by imaging conditions. This design facilitates more effective disentanglement of semantic information from imaging noise, thereby improving the generalization performance of adapted models to SPAD depth image modality.

4.4 Gate-Guided Feature Augmentation

We observe that the learned gating vector g implicitly captures the sensitivity of different feature dimensions to variations in imaging conditions. Specifically, dimensions with larger average gate values tend to exhibit smaller variations across noise levels. This observation is supported by empirical analysis in Sec. 5.3.2, where we show a negative correlation between the average gate value and the standard deviation of CLIP features across different noise levels.

Motivated by this, we propose a Gate-Guided Feature Augmentation (GGFA) strategy to further improve model robustness under limited supervision. The key idea is to inject feature perturbations in a gate-informed manner, where the perturbation strength for each feature dimension is proportional to $(1 - g)$, encouraging the model to be robust to variations from imaging conditions.

The overall GGFA workflow is as follows. We first train the Noise Adapter without GGFA, obtaining a learned noise gate. In a second training stage, we freeze the noise gate and use it to guide feature augmentation. Specifically, for each original visual feature v, we add controlled random noise to generate an augmented feature as Eq. 6:

$$v_{\text{aug}}[i] = v[i] + \alpha \cdot (1 - g[i]) \cdot \epsilon_i, \quad \epsilon_i \sim \mathcal{N}(0,1), \tag{6}$$

where α is a global scaling factor that controls the overall perturbation strength, and $(1 - g)$ determines the dimension-wise noise scaling based on the gate. Since the gating network will further affect the noise distribution, we pass the perturbed feature v_{aug} through the noise gate to obtain the final augmented modulated feature, $v'_{\text{aug}} = v_{\text{aug}} \odot g + v_{\text{aug}}$.

During this augmentation phase, we freeze the noise gate parameters and only train the classifier on both original and augmented features. For each augmented feature, we randomly sample a noise embedding to generate the corresponding gate vector g. This design prevents the degradation of the previously learned noise-aware modulation and ensures that the classifier is exposed to a broader range of noise-conditioned feature variations. The training objective is a standard cross-entropy loss computed over both the original and augmented samples in each iteration. This two-stage strategy enables the model to learn robust decision boundaries that generalize better across a spectrum of realistic noise-induced feature variations, while preserving the noise-aware feature modulation introduced by the Noise Adapter.

5 Experiments

5.1 Experimental Setup

Dastaset: We evaluate our method on both synthetic and real SPAD datasets comprising 11 categories introduced in the prior work (Zhang et al., 2025). The **synthetic SPAD dataset** is generated by simulating single-photon histograms from RGB-D images. It contains about 33,000 samples across 11 object classes. To align the spatial sparsity of SPAD imaging, all simulated images are downsampled to a resolution of 128×72 pixels. The **real SPAD dataset** contains 4,400 reconstructed depth images spanning the same 11 categories as the synthetic dataset. Each class includes 400 single-photon samples. The depth image is reconstructed using the SSPI algorithm (Yao et al., 2022) with a resolution of 64×64 pixels.

Implementation Details: We evaluate our method on both synthetic and real single-photon datasets, splitting each dataset into training, validation, and test subsets with a ratio of 0.6:0.1:0.3. All methods use the pre-trained CLIP ViT-B/32 model as the visual feature encoder. To ensure a fair comparison, all trainable models are optimized using the AdamW optimizer with an initial learning rate of 0.001, batch size of 64, and a cosine annealing learning rate schedule over 100 epochs.

Following prior work, we evaluate performance under different data-scarce scenarios by selecting 1, 2, 4, 8, and 16 labeled samples per class for training (Zhang et al., 2022; Gao et al., 2024). Each experiment is repeated with 5 different random seeds. For each run, the data split is regenerated following the specified ratio. We report the mean classification accuracy and standard deviation across these runs.

In our proposed Noise Adapter, both the noise-gating module and the classification head are implemented as two-layer MLPs. The hidden dimension of each MLP is set equal to the feature dimension of the CLIP visual encoder output.

Baseline: (1) Linear-probing: trains a linear classifier on top of the frozen visual encoder using the few-shot labeled samples; (2) Tip-Adapter: a training-free adapter that builds a key-value cache from support features and combines visual-textual similarities by tuning their weights on the validation set (Zhang et al., 2022); (3) Tip-Adapter-F: fine-tunes the cached visual embeddings while also searching for the optimal combination of visual and textual similarity weights using the validation set (Zhang et al., 2022); (4) CLIP-Adapter: trains a two-layer MLP to adapt visual features and combines them with CLIP text features, weights are tuned on the validation set for best fusion (Gao et al., 2024); (5) Meta-Adapter utilizes meta-testing mechanism and a lightweight adapter (Song et al., 2023).

5.2 Results and Analysis

Figure 3 shows the few-shot classification performance of various methods on both the synthetic SPAD dataset (Figure 3a) and the real SPAD dataset (Figure 3b). Our proposed Noise Adapter consistently outperforms all baseline methods across different numbers of labeled samples per class, especially when more training examples are available. Due to the domain shift between the RGB data used to pre-train CLIP and the SPAD depth images in our task, the zero-shot accuracy of CLIP is relatively low (Table 3 and Table 4). This domain gap also negatively impacts methods that rely heavily on CLIP's text embeddings, such as Meta-Adapter, which shows limited performance improvements even as the number of labeled samples increases. In addition, the large modality gap makes it difficult for training-free approaches like Tip-Adapter or methods that only apply minimal changes to the pre-trained features (e.g., Linear Probing), to adapt effectively, leading to suboptimal accuracy. In contrast, CLIP-Adapter and Tip-Adapter-F, which allow for more flexible adaptation of CLIP features, achieve relatively better performance.

Our Noise Adapter adopts a similar structure to CLIP-Adapter, utilizing a two-layer MLP to adapt visual features. However, it further enhances adaptation by incorporating noise embeddings extracted from SPAD raw data. These noise embeddings encode information about imaging conditions, which helps the adapter distinguish between noise-induced and semantics-induced variations in the images. As a result, the model achieves higher accuracy.

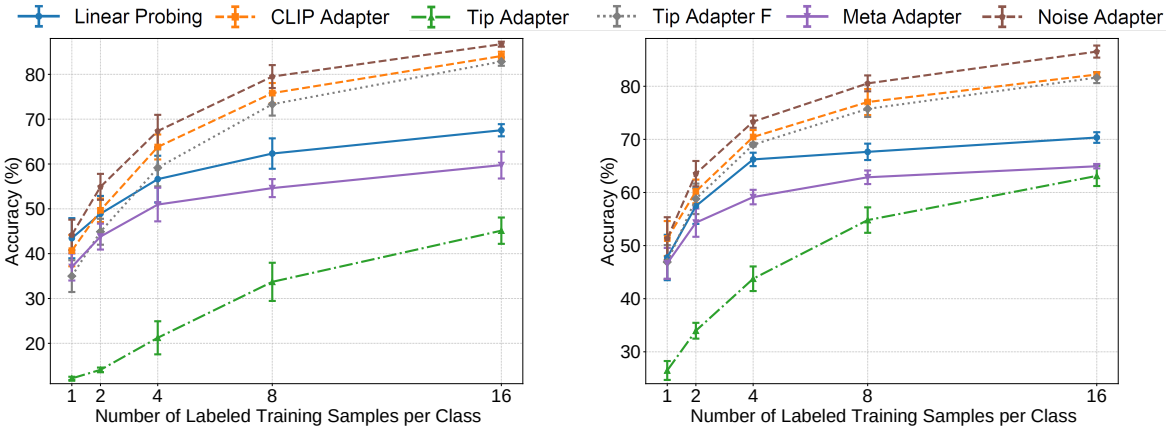

(a) Syn (b) Real

Figure 3: Few-shot classification accuracy comparison on (a) synthetic and (b) real SPAD datasets. Each curve shows the average accuracy and standard deviation over 5 random trials.

As shown in Figure 3, Noise-Adapter performs comparably to other trainable adapters in the 1-shot setting, as limited data makes it challenging to learn meaningful noise-conditioned representations. However, as more training data becomes available, Noise-Adapter demonstrates significant performance gains, highlighting the benefit of modeling noise explicitly in this domain.

Performance of Different Noise Levels We further evaluate the robustness of different methods under varying noise levels on the real SPAD depth image dataset. Since the quality of SPAD depth images is highly correlated with the average number of detected photons per pixel, we partition the test samples into four groups based on their normalized average photon count. Lower photon counts (e.g., 0–0.25) correspond to lower imaging quality and higher noise levels. Figure 4 shows the performance of all methods across different photon count ranges under 2-shot, 4-shot, 8-shot, and 16-shot settings. Across all methods, prediction accuracy generally improves as photon count increases, confirming that photon noise significantly impacts classification performance in SPAD depth images.

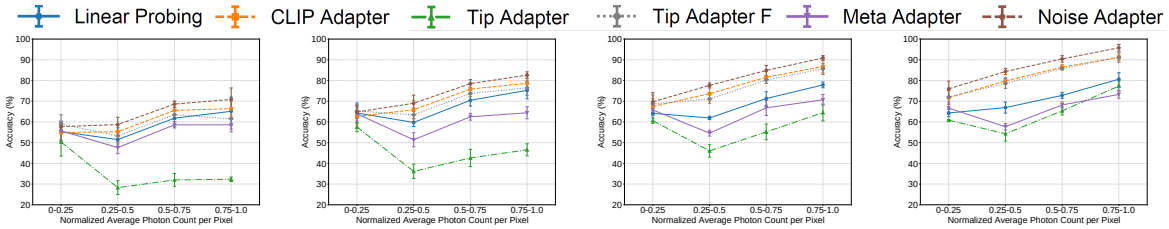

(a) 2 shots (b) 4 shots (c) 8 shots (d) 16 shots

Figure 4: Classification accuracy of our method and baselines under different noise levels of the real SPAD dataset. Each subfigure corresponds to a different few-shot setting ((a) 2, (b) 4, (c) 8, and (d) 16 shots), while the x-axis indicates four photon count intervals that represent increasing image quality. Results are averaged over 5 random trials.

In the low-shot settings (2-shot and 4-shot), our proposed Noise Adapter exhibits clear advantages over baselines in the higher photon count ranges (0.5–1.0), but performs comparably to baselines in the lowest photon count range (0–0.25). We attribute this to the limited number of labeled samples constraining the model's ability to fully learn the complex interaction between noise characteristics and semantic structure in very noisy samples. However, the explicit incorporation of noise embeddings provides the adapter with valuable information about imaging conditions, helping to improve its overall accuracy.

As the number of labeled samples increases (8-shot and 16-shot), Noise Adapter consistently achieves the best accuracy across all photon count ranges. With more supervision, the model can learn more effectively how to disentangle noise-induced variations from semantic content, enabling better generalization across both low- and high-noise samples. These results validate our hypothesis that incorporating explicit noise-awareness into the adaptation process is critical for recognizing SPAD depth images that are highly sensitive to variations in imaging conditions.

5.3 Ablation Study

To better understand the contributions of different components in our method, we conduct a series of ablation studies on the syn/real SPAD depth image datasets. The ablations are organized into two parts: model architectures and feature augmentations. In addition, we provide extended analysis in the appendix, including results across different pre-trained backbones (Appendix B) and a deeper investigation of GGFA (Appendix C).

5.3.1 Analysis of Noise Adapter architecture

First, we analyze the impact of different model architectures for incorporating noise information. We compare (1) a linear classifier trained on the CLIP visual features v, (2) a linear classifier trained on concatenated visual features and noise embeddings $[v, z]$, (3) a MLP classifier trained on the same concatenated features, and (4) our proposed Noise Adapter, which uses a noise gate to map the noise embedding into a gating vector that modulates the visual features.

As shown in Figure 5, the worst-performing variant is linear probing with noise embedding, which even underperforms standard linear probing. This suggests that directly concatenating noise embeddings to CLIP features can harm the representation, especially when the classifier lacks sufficient capacity to compensate for this disturbance (e.g. Linear probing).

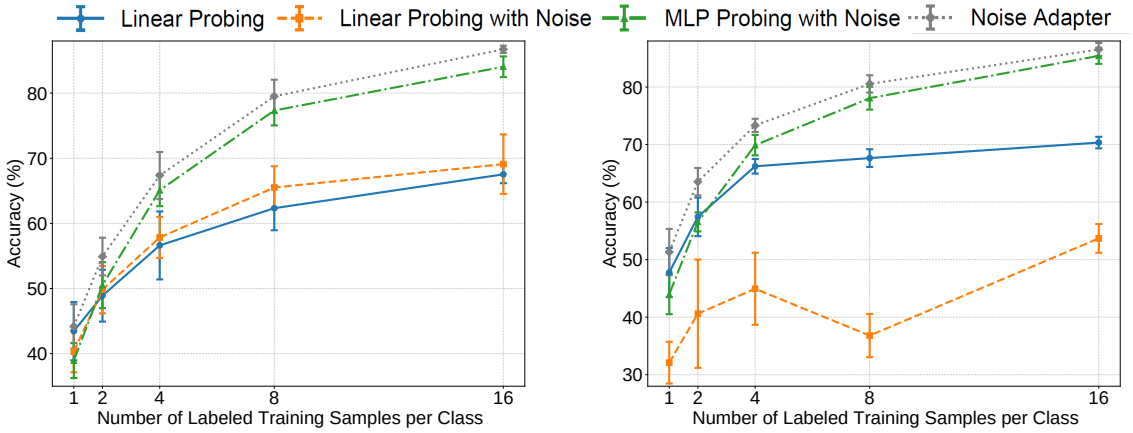

(a) Syn (b) Real

Figure 5: Ablation study comparing different ways of incorporating noise information into the classification pipeline. We compare: (1) Linear Probing, (2) Linear Probing with Noise, which concatenates noise embeddings to visual features before linear classification; (3) MLP Probing with Noise, which uses an MLP on concatenated features; and (4) our proposed Noise Adapter on (a) Syn SPAD dataset and (b) Real SPAD dataset.

MLP probing with noise performs better and is able to exploit the additional information provided by noise embeddings. However, under few-shot settings (e.g., 1-shot and 2-shot), it tends to overfit the specific noise conditions in the training samples, leading to suboptimal generalization. This result likely stems from its reliance on learning complex mappings from limited data, without a structured mechanism to separate noise-related variations from semantic cues.

In contrast, our Noise Adapter achieves consistently strong results. Under limited labeled samples, it performs on par with or better than the linear probing baseline, indicating that it preserves the semantic structure of CLIP features. As the number of labeled samples increases, the Noise Adapter shows more substantial improvements over all other variants. This demonstrates the benefit of its design: by using noise embeddings to modulate the visual features through a learnable gating mechanism, it allows the model to suppress noise-induced variations while retaining relevant semantic information. Overall, these results highlight the importance of both incorporating noise-aware signals and using them in a structured, learnable way to enhance model robustness under varying imaging conditions.

Feature Visualization To further analyze how different ways of integrating noise information impact the feature representations, we visualize the features produced by different variants using PaCMAP (Wang et al., 2021) on the real SPAD depth image dataset, as shown in Figure 6.

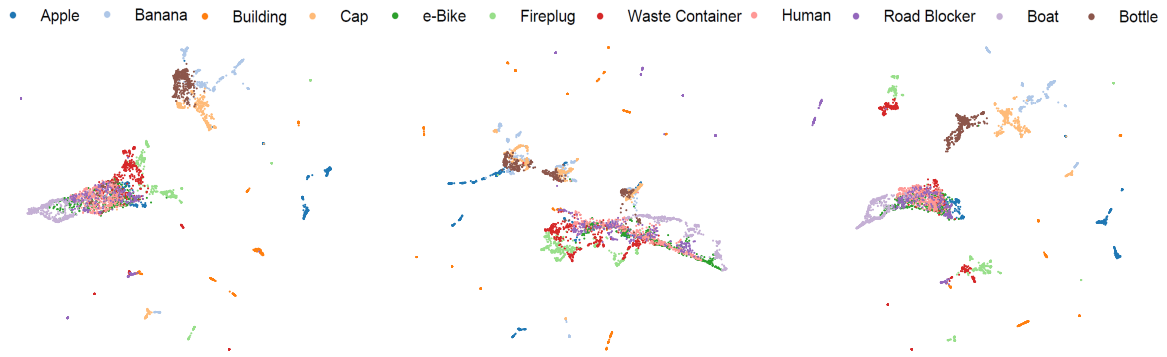

(a) CLIP visual feature v (b) Concatenated feature $[v, z]$ (c) Modulated features v'

Figure 6: PaCMAP visualization of different feature representations on the real SPAD dataset. (a) Original CLIP visual features v, (b) features obtained by concatenating CLIP features with noise embeddings $[v, z]$, and (c) features v' produced by our Noise Adapter.

In Figure 6a, the original CLIP visual features demonstrate good generalization despite being pre-trained on natural images, which are substantially different from SPAD depth images. Distinct classes form well-separated clusters, indicating that the pre-trained CLIP encoder captures transferable semantic information even under the SPAD modality.

However, as shown in Figure 6b, directly concatenating noise embeddings with CLIP visual features introduces degradation in features. The added noise embedding increases sensitivity to imaging condition variations, causing features of the same semantic class to fragment into multiple sub-clusters corresponding to different noise levels. Moreover, certain classes become less separable and exhibit overlap with other categories, suggesting that naive concatenation can amplify nuisance variation rather than helping the model to disambiguate it.

In contrast, Figure 6c shows that our Noise Adapter effectively leverages the noise embeddings through a learned gating mechanism, improving the quality of the feature space. The modulated features exhibit improved inter-class separation, indicating that the adapter successfully helps to disentangle noise-induced variation from semantic structure. This supports our design choice of using a gating-based modulation instead of direct feature concatenation, allowing the model to better preserve semantic information while adapting to varying imaging conditions.

5.3.2 Analysis of Gate-Guided Feature Augmentation

Second, we evaluate the effect of different feature augmentation strategies. We compare (1) no feature augmentation, (2) adding random noise with fixed standard deviation to the modulated features v', (3) adding random noise with fixed standard deviation to the original visual features v, and then applying the

learned noise gate to produce augmented modulated features, and (4) our full method, where the noise gate's mean values are used to determine dimension-wise noise scaling for feature augmentation.

Correlation between Gate and Feature across various noise levels We first analyze how the learned gating vector g relates to the noise sensitivity of different feature dimensions. Figure 7 shows the correlation between the average gate value and the standard deviation of CLIP visual features across different noise levels, under 1-shot, 4-shot, and 16-shot settings. Each point corresponds to one feature dimension.

A negative correlation is observed, indicating that dimensions with lower gate values tend to exhibit higher variability across noise conditions. This suggests that the gating mechanism implicitly captures per-dimension noise sensitivity, with g modulating feature robustness accordingly.

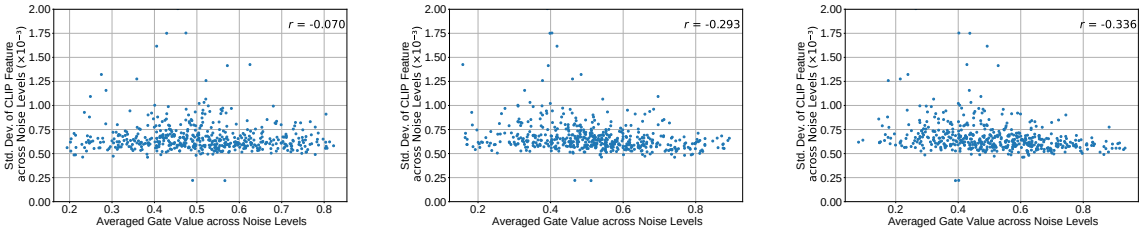

(a) 1 shot (b) 4 shots (c) 16 shots

Figure 7: Correlation between the averaged gate value and the standard deviation of CLIP features across different noise levels. Each point corresponds to one feature dimension. A negative correlation is observed, indicating that the gating mechanism tends to assign lower gate values to dimensions with higher feature variability. (a), (b), and (c) show the results under the 1-shot, 4-shot, and 16-shot settings, respectively. The correlation coefficient is computed using Spearman's rank correlation.

As shown in Figure 7, this correlation (Spearman's rank correlation (Zwillinger & Kokoska, 1999)) becomes stronger as the number of labeled samples increases. In the 1-shot setting, the correlation is weak ($r = -0.070$), likely due to insufficient supervision. However, with 4-shot and 16-shot settings, the negative correlation strengthens ($r = -0.293$ and $r = -0.336$, respectively), suggesting that the model progressively learns to align the gating pattern with feature sensitivity as more data becomes available.

These results provide empirical support for the design of our Gate-Guided Feature Augmentation (GGFA) strategy, where $(1 - g)$ is used to modulate the strength of feature perturbations. By leveraging the learned gate pattern, GGFA introduces noise-consistent variations during training, making the augmented features more closely resemble the actual feature variations observed under different imaging conditions. This encourages the classifier to generalize better to real noise-induced feature shifts.

Effect of gate-guided feature augmentation We next analyze the impact of different feature augmentation strategies on the performance of the Noise Adapter. The experiments compare variants with and without feature augmentation, as well as different noise injection schemes designed to improve the robustness of the modulated features. As shown in Table 1 and Table 2, the benefits of GGFA are more pronounced in low-shot scenarios (1-shot and 2-shot), where limited supervision makes it more important to expose the model to a diverse range of noise-conditioned feature variations. In higher-shot settings, the model can already learn such variations from the data itself, diminishing the impact of the feature augmentation.

Results show that adding random noise directly to the modulated features (Rand) does not yield noticeable performance gains. We attribute this to the fact that such augmented features deviate substantially from the true distribution of noise-modulated features. In contrast, injecting noise at the original feature level followed by gating (noise gate) produces augmented features that better match the characteristics of the modulated feature space, leading to more consistent performance improvements across both synthetic and real datasets.

Using gate-aware scaling (GGFA) further refines the augmentation process by adapting the noise strength based on the learned sensitivity of each feature dimension. However, this brings only modest gains. One

Table 1: Ablation study of Gate-Guided Feature Augmentation (GGFA) on the SPAD real dataset. Results show average accuracy with standard deviation (%) over 5 trials. The best results are shown in blue.

Few-shot Setup	1	2	4	8	16
w/o GGFA	50.39 ± 4.75	62.95 ± 2.31	73.09 ± 0.95	80.14 ± 1.68	86.61 ± 1.19
Rand	49.55 ± 5.11	62.68 ± 2.26	72.68 ± 0.62	80.36 ± 2.08	86.26 ± 1.18
Rand with Gate	51.02 ± 4.37	63.27 ± 2.53	72.97 ± 0.98	80.42 ± 2.64	86.21 ± 1.38
GGFA	51.24 ± 4.48	63.18 ± 2.70	73.15 ± 0.52	80.45 ± 2.42	86.68 ± 1.28

reason is that the correlation between the gate values and the actual feature variance across noise levels is relatively weak (Spearman correlation ≈ -0.33), as shown in Figure 7, and stronger relationships require more training data to emerge. Another factor is that the range of observed per-dimension feature variance across gate value is relatively small (typically varying from approximately 0.5×10^{-3} to 0.75×10^{-3}), which limits the potential benefit of fine-grained noise scaling. Overall, these results highlight that the structure-preserving property of gating plays a more critical role than per-dimension variance scaling in our setting.

6 Conclusion

Single-photon LiDAR offers unique advantages for long-range and low-light sensing, but semantic understanding from SPAD depth images remains challenging due to the scarcity of data and the strong impact of imaging conditions on image appearance. Addressing this challenge is critical for extending the utility of SPAD LiDAR beyond geometric reconstruction.

We propose a noise-aware adaptation framework that leverages physically interpretable noise descriptors to modulate CLIP visual features, improving generalization under varying imaging conditions. Furthermore, we observe that the learned gating patterns exhibit a correlation with feature sensitivity to noise-induced variations, which motivates our Gate-Guided Feature Augmentation (GGFA) strategy. GGFA leverages the gating pattern to generate realistic feature perturbations, further enhancing robustness under limited supervision. Extensive experiments on both synthetic and real SPAD datasets demonstrate that our method consistently outperforms existing adaptation baselines. These findings suggest that incorporating modality-aware, physically interpretable noise descriptors can significantly improve adaptation performance when transferring vision-language models to novel sensing modalities. More broadly, our results highlight the potential of using lightweight adaptation strategies to effectively extend pre-trained VLMs from RGB domains to challenging domains such as SPAD imaging.

7 Limitations and Future Directions

While our approach demonstrates strong performance improvements for SPAD depth image understanding, several limitations remain. First, the SPAD histogram data inherently contains richer information beyond what is captured by the two simple global statistics, average photon count and signal-to-background ratio, used in our current noise embedding. More sophisticated representations of the raw histogram could provide additional cues about imaging quality and noise characteristics, and may further improve adaptation performance. Exploring how to effectively incorporate this richer information and better align it with pre-trained RGB-based vision-language models is an important direction for future research.

Second, the quality of SPAD depth images at different noise levels is also influenced by the choice of the SPAD imaging algorithm. In this work, we rely on the depth images provided by the public dataset, and do not analyze how different reconstruction methods affect the learned features or the adaptation process. Studying the interaction between SPAD imaging algorithms and VLM-based adaptation remains an open area for further exploration.

References

Dylan Auty and Krystian Mikolajczyk. Learning to prompt clip for monocular depth estimation: Exploring the limits of human language. In *Proceedings of the IEEE/CVF International Conference on Computer Vision*, pp. 2039–2047, 2023.

Maria Axelsson. Semantic segmentation of persons in point clouds from photon counting lidar. In *2024 IEEE International Conference on Imaging Systems and Techniques (IST)*, pp. 1–6. IEEE, 2024.

Stanley H Chan, Hashan K Weerasooriya, Weijian Zhang, Pamela Abshire, Istvan Gyongy, and Robert K Henderson. Resolution limit of single-photon lidar. In *Proceedings of the IEEE/CVF Conference on Computer Vision and Pattern Recognition*, pp. 25307–25316, 2024.

John J Degnan. Scanning, multibeam, single photon lidars for rapid, large scale, high resolution, topographic and bathymetric mapping. *Remote Sensing*, 8(11):958, 2016.

Peng Gao, Shijie Geng, Renrui Zhang, Teli Ma, Rongyao Fang, Yongfeng Zhang, Hongsheng Li, and Yu Qiao. Clip-adapter: Better vision-language models with feature adapters. *International Journal of Computer Vision*, 132(2):581–595, 2024.

Robert H Hadfield. Single-photon detectors for optical quantum information applications. *Nature Photonics*, 3(12):696–705, 2009.

Abderrahim Halimi, Rachael Tobin, Aongus McCarthy, Jose Bioucas-Dias, Stephen McLaughlin, and Gerald S Buller. Robust restoration of sparse multidimensional single-photon lidar images. *IEEE Transactions on Computational Imaging*, 6:138–152, 2019.

Cheng Han, Qifan Wang, Yiming Cui, Zhiwen Cao, Wenguan Wang, Siyuan Qi, and Dongfang Liu. E2vpt: An effective and efficient approach for visual prompt tuning. In *2023 IEEE/CVF International Conference on Computer Vision (ICCV)*, pp. 17445–17456, 2023.

Yu Hong, Yuxiao Li, Chen Dai, Jun-Tian Ye, Xin Huang, and Feihu Xu. Image-free target identification using a single-point single-photon lidar. *Optics Express*, 31(19):30390–30401, 2023.

Tianyu Huang, Bowen Dong, Yunhan Yang, Xiaoshui Huang, Rynson WH Lau, Wanli Ouyang, and Wangmeng Zuo. Clip2point: Transfer clip to point cloud classification with image-depth pre-training. In *Proceedings of the IEEE/CVF International Conference on Computer Vision*, pp. 22157–22167, 2023.

Yunshi Huang, Fereshteh Shakeri, Jose Dolz, Malik Boudiaf, Houda Bahig, and Ismail Ben Ayed. Lp++: A surprisingly strong linear probe for few-shot clip. In *Proceedings of the IEEE/CVF Conference on Computer Vision and Pattern Recognition*, pp. 23773–23782, 2024.

Menglin Jia, Luming Tang, Bor-Chun Chen, Claire Cardie, Serge Belongie, Bharath Hariharan, and Ser-Nam Lim. Visual prompt tuning. In *European Conference on Computer Vision*, pp. 709–727. Springer, 2022.

Quentin Legros, Sylvain Meignen, Stephen McLaughlin, and Yoann Altmann. Expectation-maximization based approach to 3D reconstruction from single-waveform multispectral lidar data. *IEEE Transactions on Computational Imaging*, 6:1033–1043, 2020.

Junnan Li, Dongxu Li, Silvio Savarese, and Steven Hoi. Blip-2: Bootstrapping language-image pre-training with frozen image encoders and large language models. In *International Conference on Machine Learning*, pp. 19730–19742. PMLR, 2023.

Xiaozhe Li, Jinyi Liu, Guoyang Zhao, Lijun Liu, Weiping Zhang, Xiaomin Hu, and Shuming Cheng. High precision single-photon object detection via deep neural networks. *Optics Express*, 32(21):37224–37237, 2024.

Zheng Ping Li, Jun Tian Ye, Xin Huang, Peng Yu Jiang, Yuan Cao, Yu Hong, Chao Yu, Jun Zhang, Qiang Zhang, Cheng Zhi Peng, et al. Single-photon imaging over 200 km. *Optica*, 8(3):344–349, 2021.

Weihan Luo, Anagh Malik, and David B Lindell. Transientangelo: Few-viewpoint surface reconstruction using single-photon lidar. In *2025 IEEE/CVF Winter Conference on Applications of Computer Vision (WACV)*, pp. 8723–8733. IEEE, 2025.

Anagh Malik, Parsa Mirdehghan, Sotiris Nousias, Kyros Kutulakos, and David Lindell. Transient neural radiance fields for lidar view synthesis and 3d reconstruction. *Advances in Neural Information Processing Systems*, 36:71569–71581, 2023.

Aongus McCarthy, Gregor G Taylor, Jorge Garcia-Armenta, Boris Korzh, Dmitry V Morozov, Andrew D Beyer, Ryan M Briggs, Jason P Allmaras, Bruce Bumble, Marco Colangelo, et al. High-resolution long-distance depth imaging lidar with ultra-low timing jitter superconducting nanowire single-photon detectors. *Optica*, 12(2):168–177, 2025.

German MoraMartin, Stirling Scholes, Robert K Henderson, Jonathan Leach, and Istvan Gyongy. Human activity recognition using a single-photon direct time-of-flight sensor. *Optics Express*, 32(10):16645–16656, 2024.

Alec Radford, Jong Wook Kim, Chris Hallacy, Aditya Ramesh, Gabriel Goh, Sandhini Agarwal, Girish Sastry, Amanda Askell, Pamela Mishkin, Jack Clark, et al. Learning transferable visual models from natural language supervision. In *International Conference on Machine Learning*, pp. 8748–8763. PMLR, 2021.

Joshua Rapp and Vivek K Goyal. A few photons among many: Unmixing signal and noise for photon-efficient active imaging. *IEEE Transactions on Computational Imaging*, 3(3):445–459, 2017.

Joshua Rapp, Julian Tachella, Yoann Altmann, Stephen McLaughlin, and Vivek K Goyal. Advances in single-photon lidar for autonomous vehicles: Working principles, challenges, and recent advances. *IEEE Signal Processing Magazine*, 37(4):62–71, 2020.

Mingjia Shangguan, Zhifeng Yang, Zaifa Lin, Zhongping Lee, Haiyun Xia, and Zhenwu Weng. Compact long-range single-photon underwater lidar with high spatial–temporal resolution. *IEEE Geoscience and Remote Sensing Letters*, 20:1–5, 2023.

Lin Song, Ruoyi Xue, Hang Wang, Hongbin Sun, Yixiao Ge, Ying Shan, et al. Meta-adapter: An online few-shot learner for vision-language model. *Advances in Neural Information Processing Systems*, 36: 55361–55374, 2023.

Aleksi Suonsivu, Lauri Salmela, Edoardo Peretti, Leevi Uosukainen, Radu Ciprian Bilcu, and Giacomo Boracchi. Time-resolved mnist dataset for single-photon recognition. In *European Conference on Computer Vision*, pp. 127–143. Springer, 2025.

Julián Tachella, Yoann Altmann, Nicolas Mellado, Aongus McCarthy, Rachael Tobin, Gerald S Buller, Jean-Yves Tourneret, and Stephen McLaughlin. Real-time 3D reconstruction from single-photon lidar data using plug-and-play point cloud denoisers. *Nature Communications*, 10(1):4984, 2019.

Vishaal Udandarao, Ankush Gupta, and Samuel Albanie. Sus-x: Training-free name-only transfer of vision-language models. In *Proceedings of the IEEE/CVF International Conference on Computer Vision*, pp. 2725–2736, 2023.

Yingfan Wang, Haiyang Huang, Cynthia Rudin, and Yaron Shaposhnik. Understanding how dimension reduction tools work: an empirical approach to deciphering t-sne, umap, trimap, and pacmap for data visualization. *Journal of Machine Learning Research*, 22(201):1–73, 2021.

Ying Yang, Jianhong Shi, Fei Cao, Jinye Peng, and Guihua Zeng. Computational imaging based on time-correlated single-photon-counting technique at low light level. *Applied Optics*, 54(31):9277–9283, 2015.

Gongxin Yao, Yiwei Chen, Chen Jiang, Yixin Xuan, Xiaomin Hu, Yong Liu, and Yu Pan. Dynamic single-photon 3D imaging with a sparsity-based neural network. *Optics Express*, 30(21):37323–37340, 2022.

Runjia Zeng, Cheng Han, Qifan Wang, Chunshu Wu, Tong Geng, Lifu Huangg, Ying Nian Wu, and Dongfang Liu. Visual fourier prompt tuning. *Advances in Neural Information Processing Systems*, 37:5552–5585, 2024.

Xiaohua Zhai, Alexander Kolesnikov, Neil Houlsby, and Lucas Beyer. Scaling vision transformers. In *Proceedings of the IEEE/CVF conference on Computer Vision and Pattern Recognition*, pp. 12104–12113, 2022.

Renrui Zhang, Wei Zhang, Rongyao Fang, Peng Gao, Kunchang Li, Jifeng Dai, Yu Qiao, and Hongsheng Li. Tip-adapter: Training-free adaption of clip for few-shot classification. In *European Conference on Computer Vision*, pp. 493–510. Springer, 2022.

Zili Zhang, Ziting Wen, Yiheng Qiang, Hongzhou Dong, Wenle Dong, Xinyang Li, Xiaofan Wang, and Xiaoqiang Ren. Label-efficient single photon images classification via active learning. *arXiv preprint arXiv:2505.04376*, 2025.

Kaiyang Zhou, Jingkang Yang, Chen Change Loy, and Ziwei Liu. Conditional prompt learning for vision-language models. In *Proceedings of the IEEE/CVF conference on Computer Vision and Pattern Recognition*, pp. 16816–16825, 2022a.

Kaiyang Zhou, Jingkang Yang, Chen Change Loy, and Ziwei Liu. Learning to prompt for vision-language models. *International Journal of Computer Vision*, 130(9):2337–2348, 2022b.

Xiangyang Zhu, Renrui Zhang, Bowei He, Aojun Zhou, Dong Wang, Bin Zhao, and Peng Gao. Not all features matter: Enhancing few-shot clip with adaptive prior refinement. In *Proceedings of the IEEE/CVF International Conference on Computer Vision*, pp. 2605–2615, 2023.

Yan Zhu, Jianhong Shi, Xiaoyan Wu, Xialin Liu, Guihua Zeng, Jun Sun, Lulu Tian, and Feng Su. Photon-limited non-imaging object detection and classification based on single-pixel imaging system. *Applied Physics B*, 126(1):21, 2020.

Daniel Zwillinger and Stephen Kokoska. *CRC standard probability and statistics tables and formulae*. Crc Press, 1999. See Section 14.7.

A Broader Impact Statement

This work aims to enable semantic understanding of SPAD LiDAR depth images by adapting large-scale pre-trained vision-language models, such as CLIP, using a novel noise-aware adapter. SPAD LiDAR systems offer unique capabilities for depth imaging under extremely low-light or long-range conditions, making them attractive for applications such as autonomous navigation and remote sensing. However, the semantic interpretation of SPAD data remains a significant challenge due to photon-level noise and the scarcity of data. Our proposed method improves robustness and label efficiency in this setting.

The broader impact of this work is twofold:

Positive Impact: By bridging the gap between pre-trained vision-language models and photon-limited sensing, our method could facilitate intelligent perception in safety-critical environments where conventional cameras or LiDARs fail (e.g., nighttime robotics or rescue missions under adverse conditions). It also contributes toward reducing the data collection burden in new imaging modalities.

Potential Concerns: Like many general-purpose vision models, SPAD-based perception systems adapted from VLMs may inherit dataset biases from pre-training dataset, and could be misused in surveillance or military systems. Although our method is technically agnostic to downstream applications, developers and practitioners should ensure that such systems are deployed responsibly, with careful consideration of fairness, accountability, and privacy.

We encourage the community to continue exploring reliable, interpretable, and ethically sound methods for adapting foundation models to new sensing modalities.

B Influence of Pre-trained Backbone

To assess the generality of our method, we further evaluate its performance using two different CLIP visual encoders: ViT-B/16 and ResNet-50. As shown in Figure 8, our Noise-Adapter consistently outperforms all baselines across various numbers of labeled samples per class, regardless of the backbone architecture.

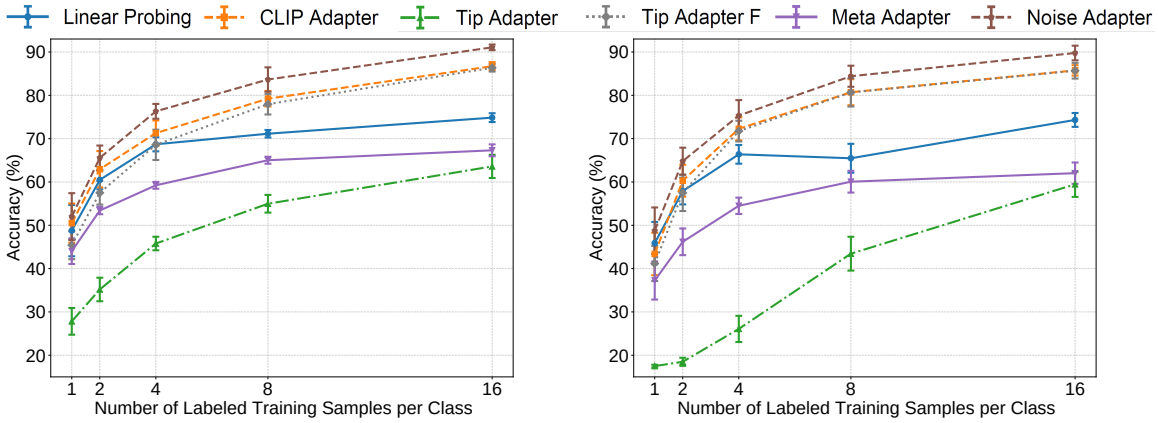

(a) ViT-B/16 (b) ResNet-50

Figure 8: Performance comparison of different methods using two CLIP pre-trained visual backbones: ViT-B/16 (a) and ResNet-50 (b). Results are reported on the real SPAD dataset across different few-shot settings, averaged over 5 random seeds.

Specifically, the overall trends observed with ViT-B/16 (Figure 8a) remain consistent when switching to ResNet-50 (Figure 8b). While the absolute accuracies vary slightly due to differences in encoder capacity and architecture, Noise-Adapter maintains a clear performance advantage across both low-shot and higher-shot regimes. This suggests that our approach is not tied to a particular encoder design and can robustly adapt to SPAD depth images across a range of vision backbones.

These results demonstrate the flexibility and generalizability of Noise-Adapter, confirming that incorporating noise-aware representations remains effective even when the underlying visual feature extractor changes.

C Additional Analysis of GGFA

The numerical results of the ablation study in the synthetic SPAD dataset are shown in table 2, where we report the average accuracy and standard deviation over 5 runs.

Table 2: Ablation study of Gate-Guided Feature Augmentation (GGFA) on the SPAD synthetic dataset. Results show average accuracy with standard deviation (%) over 5 trials. The best results are shown in blue.

Few-shot Setup	1	2	4	8	16
w/o GGFA	43.67 ± 3.61	54.53 ± 2.62	67.13 ± 3.51	79.34 ± 2.62	86.52 ± 0.60
Rand	43.49 ± 3.44	53.75 ± 3.14	67.04 ± 4.13	79.34 ± 2.55	86.71 ± 0.49
Rand with Gate	44.47 ± 3.66	54.90 ± 2.99	67.29 ± 3.66	79.46 ± 2.59	86.78 ± 0.63
GGFA	44.41 ± 3.58	54.96 ± 3.07	67.50 ± 3.71	79.48 ± 2.54	86.68 ± 0.52

C.1 Effect of Hyper-parameter α

We further analyze the sensitivity of GGFA to the perturbation strength α, which controls the magnitude of feature perturbations during augmentation. The choice of α is guided by the empirical observation that the mean standard deviation of feature dimensions in the training set is approximately 0.02. Based on this,

we vary α in the range $[0.015, 0.05]$ and evaluate the performance on the real SPAD dataset across 1-shot, 2-shot, 4-shot, 8-shot, and 16-shot settings.

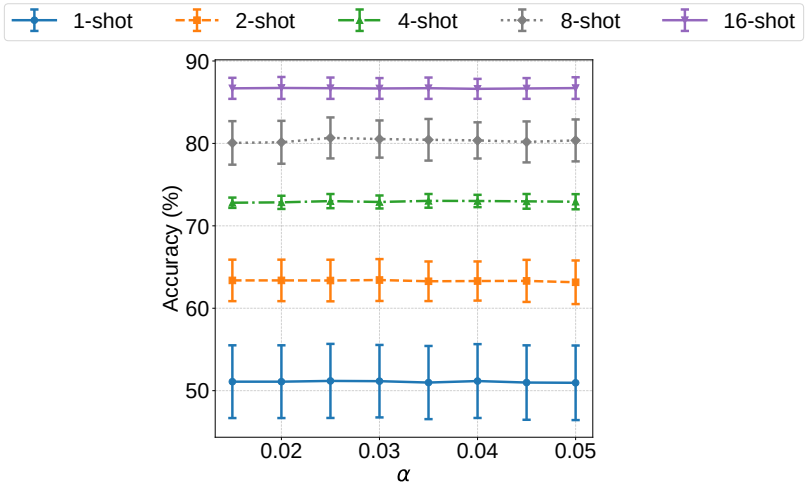

Figure 9: Sensitivity of GGFA to perturbation strength α on the real SPAD dataset. Accuracy remains stable across different α values, indicating robustness to the choice of this hyper-parameter.

Figure 9 shows that the classification accuracy remains stable across different values of α, indicating that GGFA is not sensitive to the precise choice of this hyperparameter. This robustness simplifies practical deployment, as α can be set to roughly match the average feature standard deviation without the need for extensive tuning.

C.2 Visualization Analysis of Gate-Guided Feature Augmentation

To better understand how different augmentation strategies affect feature distributions, we visualize the augmented features produced by various methods using PaCMAP on the real SPAD dataset. Specifically, we compare (a) adding uniform random noise (with $\alpha = 0.02$) directly to the modulated features, (b) adding the same random noise to the CLIP features and applying the learned noise gate to obtain augmented modulated features (Rand with Gate), and (c) our proposed GGFA method. For each method, we generate 200 augmented samples; black points indicate the augmented features in the visualizations shown in Figure 10.

As observed, directly adding random noise to the modulated features results in augmented samples that are distributed far from the original feature clusters. This likely explains why this approach fails to improve performance in Table 1, as the resulting augmented features do not resemble realistic noise-induced variations.

In contrast, both Rand with Gate and GGFA produce augmented features that are well aligned with the distribution of real features, with samples naturally scattered around the corresponding class clusters. This indicates that applying perturbations before the gating operation better preserves the underlying feature structure. Compared to Rand with Gate, GGFA tends to generate fewer augmented samples in ambiguous regions where features from multiple classes overlap, which likely reduces the introduction of unrealistic or label-ambiguous samples. This behavior may explain why GGFA achieves slightly better performance than Rand with Gate.

D Numerical Results

The numerical results of the fig. 3 in the main text are shown in table 3 and table 4, where we report the average accuracy and standard deviation over 5 runs.

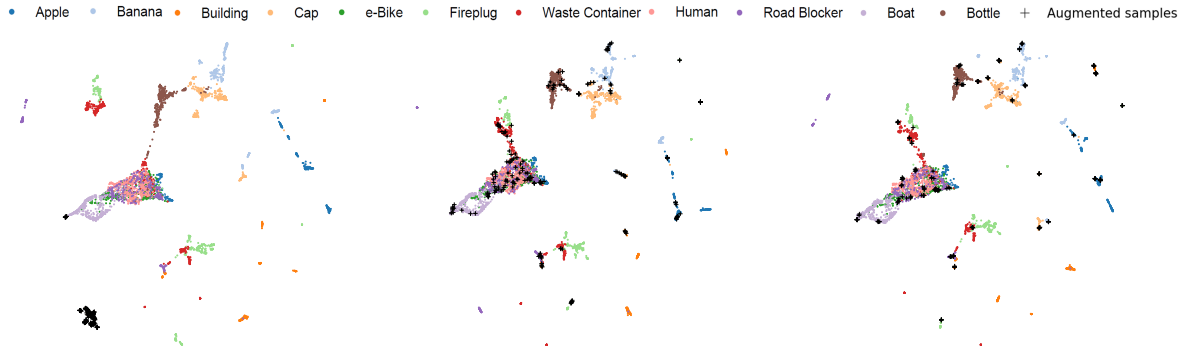

(a) Rand (b) Rand with Gate (c) GGFA

Figure 10: PaCMAP visualization of augmented features generated by different augmentation strategies on the real SPAD dataset. Black markers denote 200 augmented samples. (a) **Rand**: random noise added directly to the modulated features, (b) **Rand with Gate**: random noise added to the original CLIP features followed by gate modulation, (c) **GGFA**: noise strength is scaled by $(1 - g)$ and the resulting perturbed features are passed through the noise gate.

Table 3: Performance comparison of Noise Adaptor versus baselines on Synthetic dataset. Results show average classification accuracy with standard deviation (%) across 5 trials. The best results are shown in red and the second best results are shown in blue.

Few-shot Setup	1	2	4	8	16
CLIP Zero-shot			11.18 ± 0.14		
Tip-Adapter	12.18 ± 0.36	14.09 ± 0.51	21.23 ± 3.69	33.71 ± 4.26	45.13 ± 2.94
Tip-Adapter-F	34.99 ± 3.54	44.89 ± 2.89	59.15 ± 4.13	73.33 ± 2.53	82.85 ± 0.94
CLIP-Adapter	40.66 ± 3.48	49.68 ± 2.62	63.80 ± 2.78	75.81 ± 2.25	84.08 ± 0.96
Meta-Adapter	37.03 ± 3.01	43.81 ± 2.89	50.95 ± 3.75	54.62 ± 2.01	59.75 ± 2.99
Linear Probing	43.45 ± 4.48	48.90 ± 3.98	56.62 ± 5.22	62.33 ± 3.39	67.53 ± 1.36
Noise-Aware Adapter (ours)	44.41 ± 3.58	54.96 ± 3.07	67.50 ± 3.71	79.48 ± 2.54	86.68 ± 0.52

Table 4: Performance comparison of Noise Adaptor versus baselines on Real dataset. Results show average classification accuracy with standard deviation (%) across 5 trials. The best results are shown in red and the second best results are shown in blue.

Few-shot Setup	1	2	4	8	16
CLIP Zero-shot			18.99 ± 0.85		
Tip-Adapter	26.48 ± 1.85	33.97 ± 1.38	43.76 ± 2.84	54.80 ± 2.58	63.12 ± 1.77
Tip-Adapter-F	46.91 ± 3.18	58.80 ± 2.87	69.00 ± 0.36	75.74 ± 1.52	81.64 ± 1.04
CLIP-Adapter	51.33 ± 3.28	60.20 ± 2.23	70.45 ± 1.30	77.03 ± 2.45	82.21 ± 0.45
Meta-Adapter	46.65 ± 2.91	54.32 ± 2.66	59.14 ± 1.36	62.86 ± 1.27	64.94 ± 0.40
Linear Probing	47.76 ± 4.27	57.44 ± 3.36	66.23 ± 1.26	67.65 ± 1.54	70.35 ± 1.00
Noise-Aware Adapter (ours)	51.24 ± 4.48	63.18 ± 2.70	73.15 ± 0.52	80.45 ± 2.42	86.68 ± 1.28